RSC Advances

RSC Advances

ARTICLE

Iron metal induced deoxygenation of graphite oxide nanosheets-Insights on the capacitive properties of binder-free electrodes

Nanjundan Ashok Kumar,[a,c] Makoto Togami,[a] Yudai Oishi,[a] Masato Tominaga,[a,b] Makoto Takafuji,[a] and Hirotaka Ihara*[a,b]

An inexpensive and one-step method for the de-oxygenation of graphene oxide (GO) using iron metal powder (Fe) in strongly acidic media is reported. Considering that Fe is non-toxic compared to hydrazine, this near room temperature method is very effective in removal of most of the oxygen functionalities, as evidenced by extensive analytical characterizations. The as prepared few-layer reduced GO (rGO) were used as binder-free electrodes and their capacitive behaviours were evaluated in alkaline electrolyte. Results indicate that the electrodes exhibit much higher specific capacitance than that of the rGO produced via hydrazine or alcohol assisted reduction. With good cycling durability and electrochemical stability, the as prepared rGO electrodes shows no signs of capacitance fading for a 1000 cycles, thus promising for the fabrication of high performance additive and binder free graphene supercapacitors.

Introduction

Emerging as a material of choice, graphene has captivated the attention of research community worldwide with its remarkable properties. While the potential applications for graphene are vast, energy storage and conversion is a key arena where graphene is expected to play an important role due to its layered architecture. For such applications, bulk quantity of few-layered and exfoliated graphene is a prerequisite. A persistent challenge today, however, is to deal with ways to mass-produce them at a reasonable cost. While the search for techniques to mass-produce graphene are constantly conceived, graphene oxide (GO) is still being considered as one of the main precursors for mass production of graphene due to its versatile properties and functionalities present at their basal planes and edges that can be tuned at will. In addition to the functional properties, GO can easily be exfoliated, deoxygenated, incorporated into polymers[1, 2] and re-assembled to form novel architectures. Therefore, functionalized or reduced GO (rGO) undoubtedly provides an impetus for emerging applications.[1, 3, 4]

Up to day, GO has been de-oxygenated using various reductants such as hydrazine or hydrazine hydrate,[5] sodium borohydride,[6] zinc powder,[7] aluminum powder,[8] potassium carbonate,[9] plasma assisted reduction,[10] microwave assisted exfoliation and reduction[11] and alcohols[12] to thermal methods[13, 14] to name a few. An exhaustive list of methods and reductants used for the deoxygenation of GO can be found elsewhere.[15, 16] Although the aforementioned strategies do solve the purpose and deoxygenate GO and restore graphitic lattice, some of the reducing agents such as hydrazine are toxic and corrosive besides the incidental incorporation of nitrogen to some extent,[17] majority of the other chemical strategies to reduce GO involve multistep time-consuming processes. Thermal annealing of GO is a favored method for deoxygenation; however, high temperature treatments usually required could degrade the structural integrity of graphitic framework, apart from the process itself being energy intensive. Thus, the development simple and environmentally benign reductants to reduce GO are warranted.

While most of the rGO materials prepared previously were used for a variety of purposes, electrochemical energy storage and conversion finds top priority among various applications.[10, 18-22] Fan *et al.* first demonstrated the production of rGO by using Fe metal powder as a reducing agent and showed that such a material to possess high adsorption capacity for methylene blue (111.6mg/g),[23] thus opening avenues for the development of environmentally friendly electrode materials

for energy storage devices. Following, we compared the presence of paramagnetic metallic impurities present in rGO produced by tin induced reduction, Fe metal powder induced reduction, as well as hydrazine assisted reduction of GO using EPR technique.[24]

Complementing and detailing from the method reported by Fan *et.al.,*[23] in this work, we further reproduced predominantly large area (lateral) rGO using Fe metal powder as a reductant. The as prepared rGO was used as a binder-free electrode material for supercapacitors and their capacitive behaviors in alkaline electrolyte were evaluated in detail. Compared with alcohol reduced GO which exhibited a specific capacitance of 35 F/g,[12] and rGO obtained *via* hydrazine hydrate induced reduction with a capacitance of 51.85 F/g,[25] the as prepared additive and binder-free rGO electrodes shows significantly enhanced specific capacitance of 94 F/g in 6M KOH and 68 F/g in 0.1M KOH at a scan rate of 5 mV/s. With excellent cycling stability and durability for 1000 cycles, such a graphene material shows promising potential as electrode materials for high performance electrochemical energy storage devices.

Experimental Section

GO was synthesised from flaky graphite powder (400 nm; 99.99% metal base; impurities (quartz + mica: < 0.1%, H2O ~0.2%) by a modified Hummers and Offeman's method as described previously.[19, 26] Deoxygenation was carried out following a protocol developed by Fan *et. al.* with slight modifications.[23] Briefly, 0.6 g of GO was dispersed in 600 mL of distilled water and sonicated for an hour. Then, 6g of Fe powder (45 μm in size from Wako, Japan) was added to the mixture along with 100 mL of 35% HCl. The mixture was stirred for 30 min and left as such for 6 hours. After reduction, 75 mL of HCl was further added to remove excess Fe and the mixture was washed with copious amounts of distilled water and ethanol. Filtering using a membrane filter setup and vacuum drying at 90 °C overnight isolated the final product which was confirmed by XRD and XPS techniques.

Materials Characterization: The crystallographic structures of the materials were determined by a wide-angle X-ray diffraction system (Rigaku RAD-1B diffractometer) equipped with a reference target Cu Kα radiation operated at 35 kV, 15 mA. Raman measurements were performed on the powder samples at room temperature with a Laser-Raman spectrophotometer (NRS-5100; JASCO, Japan) at an excitation wavelength of 532 nm. Thermal decomposition patterns were determined thermogravimetrically using a TGA analyser (TG/DTA 6200; Seiko Instruments Inc,) at a ramp rate of 10°C min^{-1} in nitrogen atmosphere. X-ray photoelectron spectroscopy (XPS) measurements were carried out using a Thermo Scientific Sigma Probe spectrometer employing mono-chromatic Al Kα radiation as the X-ray source. Charging corrections were applied for the GO sample. Microstructure and

structural morphologies of the samples were investigated by a field emission scanning electron microscopy (FE-SEM SU8000, HITACHI Ltd.,) and high-resolution transmission electron microscopic (HRTEM) images were obtained using a JEOL JEM-2000FX microscope at an accelerating voltage of 200 kV.

Electrochemical measurements: For the electrochemical measurements, the rGO sample were hand mixed using an agate mortar to form a paste, which was then pressed at 1 ton on a nickel mesh (Nilaco Corporation, Tokyo, Japan) which served as a binder and additive-free working electrode. The mass loading of the active material was ~1 mg. Cyclic voltammetry measurements were carried out using an electrochemical analyser (ALS, Model 660A) employing a conventional three-electrode electrochemical cell that consisted of a graphene sandwiched nickel mesh as the working electrode, Ag/AgCl as the reference, and a platinum wire was used as the counter electrode. Experiments were carried out at room temperature in 0.1 M and 6M aqueous KOH solutions as the electrolyte at various scan rates. All potentials are reported relative to Ag/AgCl (saturated KCl) reference electrode. In order to omit the extra current generated by nickel mesh, the potential window for cycling was confined between -1.0 and 0.2 V. The voltammograms were then used to calculate the specific capacitance of the rGO by integrating over the full CV curve to determine the average area value for one cycle as reported previously.[27] Galvanostatic charge-discharge measurements of the cell were carried out between -1.0V to 0.2 V and the electrochemical impedance spectroscopy (EIS) measurement was analyzed within a frequency range of 100 kHz to 0.01 Hz at an open-circuit potential with an a.c. amplitude of 5 mV.

Results and Discussion

Oxidative breakup of graphite was carried out to introduce functional groups and to increase the inter-sheet distance to obtain exfoliated GO. Aqueous dispersions of GO were prepared from the obtained GO powder and deoxygenation process was then carried out using Fe metal powder in highly acidic media as illustrated in Scheme 1. In a typical process, Fe metal powder was added to GO dispersions followed by the addition of calculated volumes of conc. HCl while stirring. After reduction, as confirmed by the visual colour change of the aqueous dispersions from brown to black, the samples were then washed with another portion of HCl to ensure complete removal of Fe metal, therefore avoiding contamination of graphene with metal ions to a larger extent. The resulting material was further washed with copious amounts of water and ethanol and subsequently vacuum dried after filtration to yield well-deoxygenated rGO sheets.
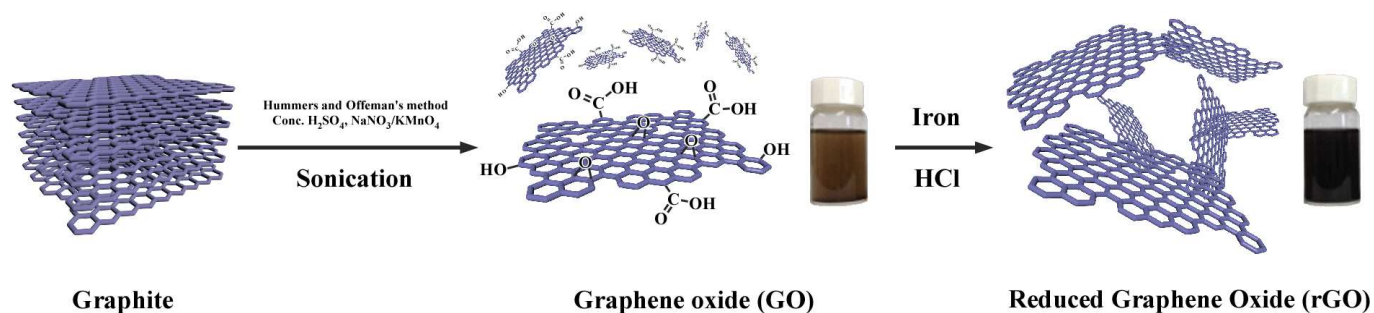
Scheme 1. Schematic cartoon of deoxygenation of graphite oxide using iron metal powder in highly acidic media

Typical morphology images of the rGO were obtained by using electron microscopic techniques namely a field emission scanning electron microscope (FE-SEM) and a high-resolution transmission electron microscope (HR-TEM). A representative FESEM image of the dry, as produced rGO powder is shown in Fig. 1a.
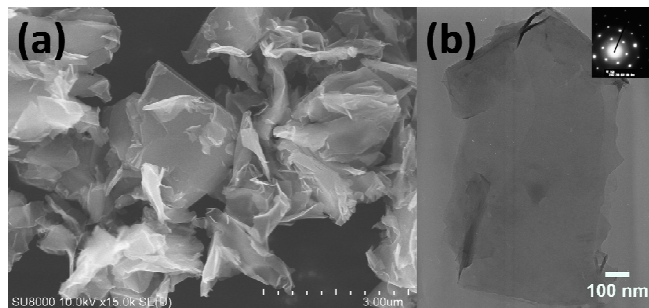

Figure 1. (a) FESEM and (b) HR-TEM morphologies of rGO. Inset in (b) shows the selected area diffraction (SAED) pattern of the sample.

Randomly corrugated, disordered and crumpled or folded sheets with minimal aggregation were observed due to the extent of reduction. Such a corrugated structure could minimize sheet restacking to a larger extent compared to that of the rGO's prepared *via* other wet chemical methods that usually tend to aggregate, thus accruing its potential for electrochemical applications. HRTEM image (Fig. 1b) obtained by dispersing a small amount of the rGO sample on copper grid show typical large area graphene sheets, which are wrinkled and corrugated especially at the edges. Careful observations of the edges show stacks of few layered graphene sheets disorderly arranged. Selected area diffraction pattern (SAED) of the rGO show ring patterns consisting of typical six membered rings indicate crystalline nature of the restored hexagonal graphene framework. The observed lattice fringes were also consistent with disordered stacking morphology suggesting effective exfoliation and further confirm the presence of few layer graphene sheets.

X-ray photoelectron microscopy (XPS) was performed to determine the degree to which graphene was deoxygenated during the reduction process in addition to obtaining the chemical composition of the material. While the small oxygen content seen in pristine graphite could originate from the surface adsorbed oxygen, the wide-scan XPS spectra of the rGO in Fig. 2a show a drastic decrease in the oxygen content after the reduction process. The high-resolution C1s spectrum of GO clearly indicate considerable degree of oxidation with two separated peaks corresponding to large amounts of sp^3 carbon with a high percentage of oxygen-containing functionalities. The C1s spectrum of GO were deconvoluted according to the method reported by Koinuma *et. al.,* previously.[28] The peak components in GO with binding energies at about 284.63, 285.03, 285.53, 286.43, 287.23, 287.73 and 288.83 eV can be attributed to carbon atoms in different functional groups such as C-C (sp^2), CH defect, C-C (sp^3), C-OH, C-O-C, C=O and O=C-O respectively (Fig. 2b).[28] Meanwhile, the peak components in rGO with binding energies at about 284.69, 286.5, 288.31, 290.61 could be ascribed to the C=C, C-O, C=O and O=C-O groups respectively (Fig 2c). The prominent C1s peak observed at 284.69 (C=C) eV in rGO indicates the sp^2 graphitic nature of the sample, suggesting a high degree of de-oxygenation after the reduction process. Unlike GO, the heterocarbon component in the C1s peak arising from C-O, C=O and O=C-O were not pronounced in the rGO sample further confirming the removal of most of the oxygen containing functional groups. The carbon to oxygen (C/O) atomic compositions determined by taking the ratios of C1s to O1s peak areas was found to be 8.3 for the rGO compared to 2.4 for the starting GO, suggesting an effective deoxygenation (an increase in the C/O ratio indicates efficient reduction of GO to rGO). It should be noted that the C/O ratios obtained here are significantly higher than that obtained *via* sodium borohydride reduction (5.3),[6] hydrothermal method (5.6),[29] solvothermal reduction and sample annealing (6.03)[30] as well as low temperature thermal reduction method (4.7).[31] In addition the value reported here is slightly higher and comparable to that of the value reported by Fan *et. al.* (7.9).[23]
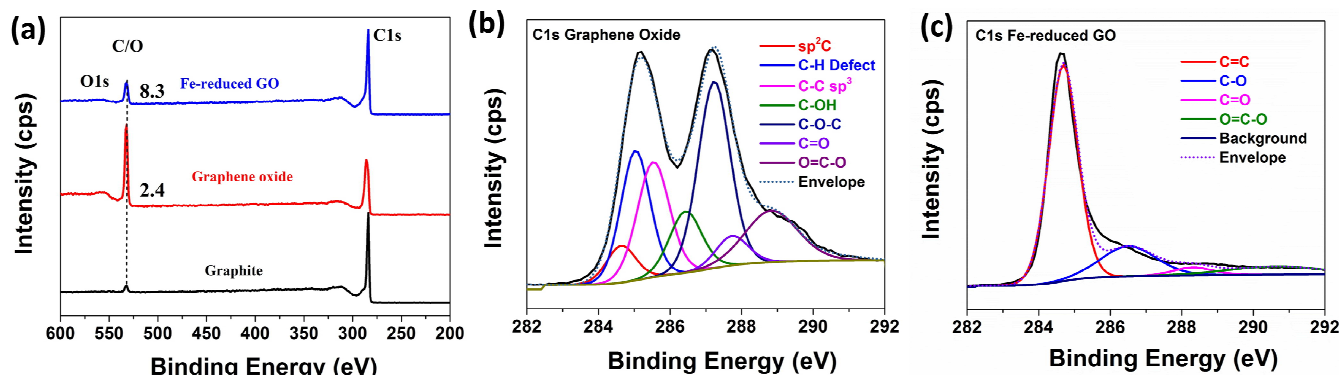
Figure 2. (a) XPS Survey scans, (b) high-resolution C1s region of GO and (c) C1s region of rGO.

In order to understand the crystallographic structural characteristics of the samples, XRD patterns of bulk graphite, GO and rGO prepared were acquired (Fig. 3a). Congruent with the XPS results, XRD shows the removal of oxygen functionalities and also elucidated the crystalline nature of the graphene sheets obtained. While pristine graphite showed a very strong 2θ peak [002] at around 26° with an interlayer spacing (*d*-spacing) of ~0.34 nm, GO exhibits a distinct and a typical diffraction peak, 2θ centered at around 11.24° corresponding to a markedly large interlayer distance of ~0.79 nm (calculated using Braggs equation). This can be attributed to the exfoliation, water intercalation and the formation of hydroxyl, carboxyl, and epoxyl functional groups on the surfaces and basal edges of the sheets. The reduced form on the other hand shows a very broad peak at 24.54° which corresponds to the [002] hexagonal plane, similar to that of a typical graphite/graphene lattice without any GO peaks, usually associated with the ring opening of epoxides. In addition, the interlayer distance of the rGO decreases to 0.36 nm, fairly close to native graphite values, primarily due to the removal of the oxygen containing functionalities. This suggests a high degree of exfoliation and re-establishment of the conjugated sp^2 networks in the lattice to a larger extent (Fig. 3a). Disorder created in the lattice structure during the oxidative breakup of graphite and reduction leading to further corrugated structures could cause the broadness of the diffraction peaks as seen here.

Raman spectroscopy, a powerful, non-destructive and a widely used tool, generally reveals the structural changes and the electronic conjugation states of graphene-based materials. For functionalized graphene materials, this technique is well documented and significantly useful in determining the number of graphene layers present aside from distinguishing ordered and disordered lattice structures. Raman spectra of pristine graphite, GO and the rGO are shown in Fig. 3b. Significant structural changes are manifested during the reduction processing. While a single and prominent G peak corresponding to first order scattering of E_{2g} mode of sp^2

carbon atoms is observed for pristine graphite at *ca.* 1568 cm^{-1}, the Raman spectrum of GO shows a broadened and a shifted G peak at *ca.* 1577 cm^{-1}. In addition to the G peak, a prominent defect band (D peak) arising from the breathing mode of k-point phonons of the A_{1g} symmetry at *ca.* 1342 cm^{-1} is also observed with substantially increased intensity. Here, the appearance of defect band is typically associated with the high edge defect concentrations originating from oxidative breakup of graphite and extensive soinication of GO to obtain homogeneous dispersions before the reduction process, resulting in lattice distortions and reduction in size of in-plane sp^2 domains.[24] Post reduction, the intensity of the 2D band arising from the second order of zone-boundary phonons in rGO at *ca.* 2674 cm^{-1} increased more significantly than those of GO, demonstrating increased graphitization. In addition, the splitting of the 2D peak reveals the disordered stacking of the lattices consisting of a mixture of single and few-layer graphene sheets.

Comparisons of the relative intensities of the D and G bands can usually indicate the change in electronic conjugation state. A higher intensity ratio after reduction usually suggests the formation of smaller in-plane sp^2 domains with an increase in disorder degree -*vide supra*- (intensity ratio is proportional to the average size of the sp^2 domains). As expected, an increased ID/IG ratio for rGO was observed (1.11) compared to that of GO (1.04). Although the intensity ratios does not decrease as reported earlier by Fan *et.al.,* the ratio number obtained here is still far less than that of values reported for hydrazine-assisted reduction (1.44),[29] implying that the graphene domains produced *via* this method is still better or comparable to hydrazine assisted reduction method, aside from being fairly environmentally friendly process. One possible reason for the variation of the intensity ratios could be attributed to the nature and size of parental graphite used for synthesizing GO. In this case, 400 nm graphite flakes was used which is smaller in size compared to other reports using a larger mesh size for example.
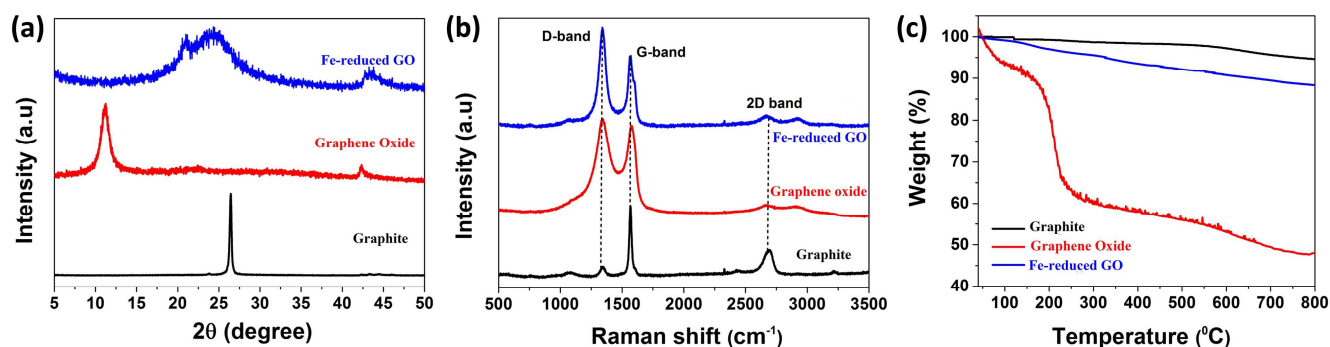
Figure 3. XRD patterns (a), Raman spectra (b) and TGA thermograms of graphite, GO and rGO.

Thermogravimetric analysis (TGA) was performed under nitrogen atmosphere to further assess the level of reduction and also to study the thermal stabilities of the parental graphite, GO and rGO sheets as shown in Fig. 3c. While graphite does not show any major mass loss up to 600 °C, a thermally unstable GO on the other hand starts to lose mass upon heating. Below 200 °C, a significant mass loss occurs as a result of the evaporation of interlamellar water followed by a major loss due to the pyrolysis of labile oxygen-containing functionalities, thereby yielding CO, CO_2 and stream at slightly higher temperatures. Around 50 % of the total mass was lost at 800 °C for the GO sample. The rGO sample showed much higher thermal stability with a negligible loss below 200 °C and a total mass loss of less than 10% was observed until 800 °C. This clearly demonstrates that the thermal stability of rGO has been increased dramatically due to the deoxygenation of the thermally labile oxygen-containing functional groups in the GO to a larger extent resulting in better graphitization.

The amount of information gleaned form the suit of analytical techniques described above proves effective deoxygenation of GO using Fe metal powder. Further, the obtained information on the nature of the multi-layer graphene material with a few persisting topological defects also shed light that this material could possess excellent super-capacitive properties. While complementing the study conducted by Fan *et. al.* previously, the objective of the present study was to evaluate the fundamental and basic electrochemical capacitive behaviours of such a well reproducible and reasonably scalable graphene material. Is it instructive to note that most of the electrode making techniques reported thus far generally involve the use of glassy carbon electrodes, or other techniques that need a great deal of precision in handling, as a tiny error in the active material mass could lead to erroneous capacitance values. In addition, the requirement of a binder and, or an additive is also a prerequisite in many such configurations. Therefore, a simple and straightforward electrode formulation procedure that does not involve the addition of a binder or an additive, is not only practical, but also industrially significant, as the practice of using thick electrodes is a norm at industrial standards for manufacturing end user products.[18] Thus, the

working electrode was fabricated by simply grinding the rGO in an agate mortar without the use of any binder or additive or a solvent to form a cohesive paste that was sandwiched in between a nickel mesh. The manufactured electrode was pressed and used.

Cyclic voltammetry (CV) that is recognised as the principle method to examine the capacitive behaviour was measured in a three-electrode system at various scan rates in a potential range between -1.0 V to 0.2 V. Well defined, near-rectangular shapes of CV curves were observed at different scan rates (Fig. 4a and Fig. 4b) indicative of excellent electrical double-layer capacitive behaviour with good charge propagation within the electrodes.
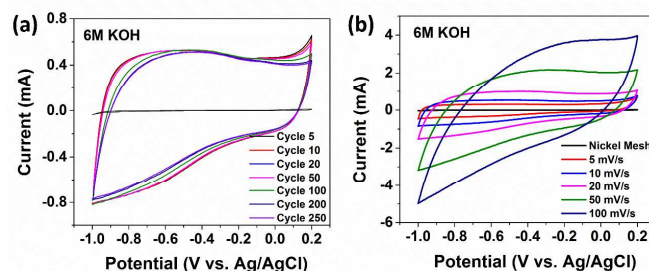

Figure 4. (a) Cyclic voltammograms (CV) recorded at 10 mV/s showing excellent cyclibility for 250 cycles. (b) CVs at various scan rates in a 6M KOH electrolyte show electrochemical double layer capacitance (EDLC) behaviour.

Although rGO materials with existing few functional groups are more likely to contribute a little pseudocapacitance, the linear current measured in the rGO electrodes indicates largely non-faradaic nature of the device, which is in line with previous reports.[32] The specific capacitance was quantified using CV curves after subtracting the negligible values of bare nickel mesh. Scan rate dependent specific capacitances were noticed for the rGO electrodes, which were determined to be 94, 83, 72 and 52 F/g at a scan rate of 5, 10, 20 and 50 mV/s respectively in a 6M KOH electrolyte (Fig. 4a and Fig. 4b). The highest specific capacitance of 94 F/g at 5 mV/s observed for the rGO

material, is consistent with those that have been reported in recent literature. For instance, a specific capacitance of 100 F/g for a hydrazine monohydrate reduced rGO in a 5.5M KOH electrolyte at 20 mV/s was reported by Stoller *et.al.* previously.[33] In addition, our values are also comparable to the pioneering work reported earlier by CNR Rao *et.al.,* where GO was thermally reduced at 1050 °C to obtain a specific capacitance as high as 117 F/g in aqueous H_2SO_4 electrolyte,[34] and also for hydrazine reduced GO in an ionic liquid electrolyte (115 F/g at 20 mV/s).[35] The electrodes were also very stable for over 250 cycles as shown in Fig. 4a with negligible capacitance loss.

The electrodes were also tested in a 0.1 M KOH electrolyte (Fig. 5). The shape of the CV curve is again near rectangular even at higher scan rates indicating excellent capacitive behaviour of the rGO material with low contact resistance.[36] A specific capacitance as high as 68 F/g at a scan rate of 5 mV/s was observed. Scan rate dependent specific capacitances of the rGO electrodes were calculated to be 68, 62, 56 and 46 F/g at a scan rate of 5, 10, 20 and 50 mV/s respectively (Fig. 5b). An insight provided earlier by Zhang and co-workers on the capacitive properties of hydrazine reduced GO in aqueous 2M H_2SO_4 electrolyte shows highest capacitance of 51.85 F/g.[25] Therefore, the values reported in the current study are better or comparable to that of other reports as discussed earlier. The decrease in specific capacitance with increasing scan rate in neither concentration of electrolytes could be attributed to the inaccessibility of the electrolyte ions to the interior surfaces of the active material because of the reduced diffusion time at higher scan rates. This common phenomenon is widely acknowledged in recent literature.
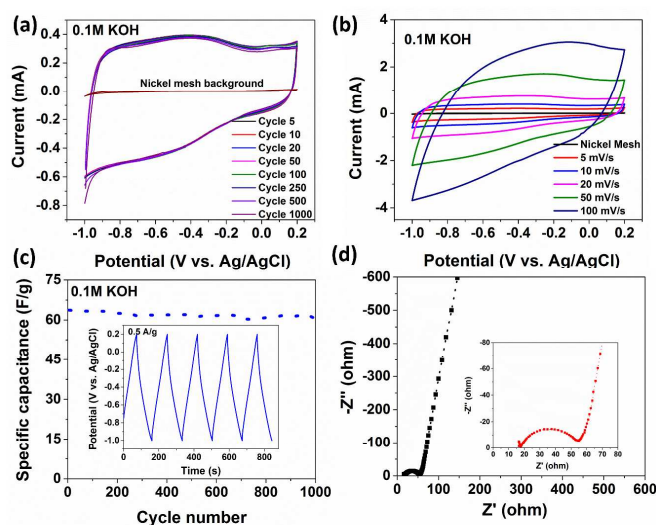
The charge-discharge profiles presented in Fig. 5c shows an ideal triangle shape suggest fast charge mobility at the electrode/electrolyte interface. Linear in the total range of potential with constant slopes indicate excellent capacitive behaviour of the rGO material with good reversibility during the charging and discharging process. The absence of *iR* drop (voltage drop) at the beginning of discharge curve suggests a low and negligible internal resistance, an evidence of the removal of majority of the oxygen-containing functional groups. As long cycle life of a supercapacitor device is critical for practical applications, the stability of graphene capacitor was evaluated for 1000 cycles. Fig. 5c shows the variation of specific capacitance with cycle number recorded at 10 mV/s. As can be seen the specific capacitance still remains almost constant for 1000 cycles of testing, illustrating good stability of the electrodes with a high degree of reversibility. The Nyquist plot of the rGO supercapacitor electrode shows an arc in the high-frequency region (inset of Fig. 5d) and a straight line in the low-frequency region (Fig. 5d). While the near vertical shape at the low-frequency region indicates near perfect and ideal capacitive behaviour of the rGO material, the low electronic resistance between the graphene sheets can be attributed to the inconspicuous arc in the high frequency region. A short Warburg resistance on the Nyquist plots that pertains to ion diffusion and transport in the electrolyte is also noticed. All the above results highlight the suitability of iron-assisted rGO material for the development of efficient and stable high performance supercapacitors. Unique advantage mainly being environmentally friendly and comparable or better performances to rGO 's obtained by other means of reduction.

Conclusions

In summary, we have studied the capacitive behaviours of rGO produced by iron metal induced reduction of GO. Suits of analytical techniques reveal that majority of the oxygen functionalities were removed leading to better graphitization. Compared to rGO prepared using hydrazine and alcohols as a reductant, the rGO prepared herein shows comparable or better capacitive performances. When used as an additive and binder-free electrode, the material exhibited a specific capacitance as high as 68 F/g in 0.1M KOH and 94 F/g in 6M KOH at a scan rate of 5 mV/s with excellent cycling stability without any decrease in specific capacitance at 1000 cycles. While further studies and optimization would be necessary to increase the specific capacitance, we believe that the fundamental study reported here will lead to further scrutinzation of the material for electrochemical energy storage and conversion devices in different electrolytes and different electrode configurations.

Figure 5. (a) Cyclic voltammograms (CV) recorded at 10 mV/s showing excellent cyclibility for 1000 cycles. (b) CVs obtained at various scan rates. (c) Specific capacitance as a function of cycle number with inset showing the chronopotentiograms (charge-discharge profiles) obtained at 0.5 A/g and (d) Nyquist plot of the rGO electrode in a 0.1M KOH electrolyte (inset shows low frequency region).

Acknowledgements

Notes and references

[a] Department of Applied Chemistry and Biochemistry, Kumamoto University, 2-39-1 Kurokami, Chuo-ku, Kumamoto, 860-8555, Japan
E-mail: ihara@kumamoto-u.ac.jp
[b] Kumamoto Institute for Photo-Electro Organics (PHOENICS), 3-11-38 Higashimachi, Kumamoto, 862-0901, Japan
[c] School of Chemical Engineering, The University of Queensland, St. Lucia, 4072, Brisbane, Australia (Present address)

1. N. Ashok Kumar and J. B. Baek, *Chem. Commun.*, 2014, **50**, 6298-6308.
2. N. A. Kumar, H. J. Choi, A. Bund, J. B. Baek and Y. T. Jeong, *J. Mater. Chem.*, 2012, **22**, 12268-12274.
3. H.-J. Choi, N. Ashok Kumar and J.-B. Baek, *Nanoscale*, 2015, doi:10.1039/C1034NR06831A.
4. N. A. Kumar, M. A. Dar, R. Gul and J.-B. Baek, *Materials Today*, 2015, doi:10.1016/j.mattod.2015.1001.1016.
5. S. Stankovich, D. A. Dikin, R. D. Piner, K. A. Kohlhaas, A. Kleinhammes, Y. Jia, Y. Wu, S. T. Nguyen and R. S. Ruoff, *Carbon*, 2007, **45**, 1558-1565.
6. H.-J. Shin, K. K. Kim, A. Benayad, S.-M. Yoon, H. K. Park, I.-S. Jung, M. H. Jin, H.-K. Jeong, J. M. Kim, J.-Y. Choi and Y. H. Lee, *Adv. Funct. Mater.*, 2009, **19**, 1987-1992.
7. X. Mei and J. Ouyang, *Carbon*, 2011, **49**, 5389-5397.
8. Z. Fan, K. Wang, T. Wei, J. Yan, L. Song and B. Shao, *Carbon*, 2010, **48**, 1686-1689.
9. D. He, Z. Peng, W. Gong, Y. Luo, P. Zhao and L. Kong, *RSC Advances*, 2015, **5**, 11966-11972.
10. N. A. Kumar, H. Nolan, N. McEvoy, E. Rezvani, R. L. Doyle, M. E. G. Lyons and G. S. Duesberg, *J. Mater. Chem. A*, 2013, **1**, 4431-4435.
11. Y. Zhu, S. Murali, M. D. Stoller, A. Velamakanni, R. D. Piner and R. S. Ruoff, *Carbon*, 2010, **48**, 2118-2122.
12. D. R. Dreyer, S. Murali, Y. Zhu, R. S. Ruoff and C. W. Bielawski, *J. Mater. Chem.*, 2011, **21**, 3443-3447.
13. M. J. McAllister, J.-L. Li, D. H. Adamson, H. C. Schniepp, A. A. Abdala, J. Liu, M. Herrera-Alonso, D. L. Milius, R. Car, R. K. Prud'homme and I. A. Aksay, *Chem. Mater.*, 2007, **19**, 4396-4404.
14. C. D. Zangmeister, *Chem. Mater.*, 2010, **22**, 5625-5629.
15. S. Pei and H.-M. Cheng, *Carbon*, 2012, **50**, 3210-3228.
16. C. K. Chua and M. Pumera, *Chem. Soc. Rev.*, 2014, **43**, 291-312.
17. S. A. Hasan, E. K. Tsekoura, V. Sternhagen and M. Strømme, *J. Phys. Chem. C*, 2012, **116**, 6530-6536.
18. B. P. N. Nguyen, N. A. Kumar, J. Gaubicher, F. Duclairoir, T. Brousse, O. Crosnier, L. Dubois, G. Bidan, D. Guyomard and B. Lestriez, *Adv. Energy Mater.*, 2013, **3**, 1351-1357.
19. N. A. Kumar, H.-J. Choi, Y. R. Shin, D. W. Chang, L. Dai and J.-B. Baek, *ACS Nano*, 2012, **6**, 1715-1723.
20. A. Ghosh and Y. H. Lee, *ChemSusChem*, 2012, **5**, 480-499.
21. D. S. Su and R. Schlogl, *ChemSusChem*, 2010, **3**, 136-168.
22. J. Zhang and X. S. Zhao, *ChemSusChem*, 2012, **5**, 818-841.
23. Z. J. Fan, W. Kai, J. Yan, T. Wei, L. J. Zhi, J. Feng, Y. M. Ren, L. P. Song and F. Wei, *ACS Nano*, 2011, **5**, 191-198.
24. N. A. Kumar, S. Gambarelli, F. Duclairoir, G. Bidan and L. Dubois, *J. Mater. Chem. A*, 2013, **1**, 2789 - 2794.
25. W. Zhang, Y. Zhang, Y. Tian, Z. Yang, Q. Xiao, X. Guo, L. Jing, Y. Zhao, Y. Yan, J. Feng and K. Sun, *ACS Appl. Mater. Interfaces*, 2014, **6**, 2248-2254.
26. W. S. Hummers and R. E. Offeman, *J. Am. Chem. Soc.*, 1958, **80**, 1339-1339.
27. N. A. Kumar, I.-Y. Jeon, G.-J. Sohn, R. Jain, S. Kumar and J.-B. Baek, *ACS Nano*, 2011, **5**, 2324-2331.
28. M. Koinuma, H. Tateishi, K. Hatakeyama, S. Miyamoto, C. Ogata, A. Funatsu, T. Taniguchi and Y. Matsumoto, *Chem. Lett.*, 2013, **42**, 924-926.
29. Y. Zhou, Q. Bao, L. A. L. Tang, Y. Zhong and K. P. Loh, *Chem. Mater.*, 2009, **21**, 2950-2956.
30. S. Dubin, S. Gilje, K. Wang, V. C. Tung, K. Cha, A. S. Hall, J. Farrar, R. Varshneya, Y. Yang and R. B. Kaner, *ACS Nano*, 2010, **4**, 3845-3852.
31. W. Chen and L. Yan, *Nanoscale*, 2010, **2**, 559-563.
32. T. Y. Kim, H. W. Lee, M. Stoller, D. R. Dreyer, C. W. Bielawski, R. S. Ruoff and K. S. Suh, *ACS Nano*, 2010, **5**, 436-442.
33. M. D. Stoller, S. Park, Y. Zhu, J. An and R. S. Ruoff, *Nano Lett.*, 2008, **8**, 3498-3502.
34. S. R. C. Vivekchand, C. S. Rout, K. S. Subrahmanyam, A. Govindaraj and C. N. R. Rao, *J. Chem. Sci.*, 2008, **120**, 9-13.
35. C. Fu, Y. Kuang, Z. Huang, X. Wang, Y. Yin, J. Chen and H. Zhou, *J. Solid State Electrochem.*, 2011, **15**, 2581-2585.
36. Y. Wang, Z. Shi, Y. Huang, Y. Ma, C. Wang, M. Chen and Y. Chen, *J. Phys. Chem. C*, 2009, **113**, 13103-13107.